Fundamental Spin Interactions Underlying the Magnetic Anisotropy in the Kitaev Ferromagnet CrI_3

Inhee Lee,[1,*] Franz G. Utermohlen,[1] Daniel Weber,[2] Kyusung Hwang,[1,3] Chi Zhang,[1] Johan van Tol,[4] Joshua E. Goldberger,[2] Nandini Trivedi,[1] and P. Chris Hammel[1,†]

[1]*Department of Physics, The Ohio State University, Columbus, Ohio 43210, USA*
[2]*Department of Chemistry and Biochemistry, The Ohio State University, Columbus, Ohio 43210, USA*
[3]*School of Physics, Korea Institute for Advanced Study, Seoul 130-722, Korea*
[4]*National High Magnetic Field Laboratory, Florida State University, Tallahassee, Florida 32310, USA*

(Received 29 January 2019; published 2 January 2020)

We lay the foundation for determining the microscopic spin interactions in two-dimensional (2D) ferromagnets by combining angle-dependent ferromagnetic resonance (FMR) experiments on high quality CrI_3 single crystals with theoretical modeling based on symmetries. We discover that the Kitaev interaction is the strongest in this material with $K \sim -5.2$ meV, 25 times larger than the Heisenberg exchange $J \sim -0.2$ meV, and responsible for opening the $\sim$5 meV gap at the Dirac points in the spin-wave dispersion. Furthermore, we find that the symmetric off-diagonal anisotropy $\Gamma \sim -67.5$ μeV, though small, is crucial for opening a $\sim$0.3 meV gap in the magnon spectrum at the zone center and stabilizing ferromagnetism in the 2D limit. The high resolution of the FMR data further reveals a μeV-scale quadrupolar contribution to the $S = 3/2$ magnetism. Our identification of the underlying exchange anisotropies opens paths toward 2D ferromagnets with higher T_C as well as magnetically frustrated quantum spin liquids based on Kitaev physics.

DOI: 10.1103/PhysRevLett.124.017201

Two-dimensional (2D) van der Waals (vdW) ferromagnets [1,2] have recently emerged as an exciting platform for the development of 2D spintronic applications [3,4] and novel 2D spin order [5,6]. These 2D ferromagnets must have magnetic anisotropy, since the Mermin-Wagner theorem forbids 2D materials with a continuous spin-rotation symmetry from spontaneously magnetizing at finite temperature [7]. Understanding 2D ferromagnets thus requires a thorough knowledge of this anisotropy. However, it remains an open question which fundamental magnetic interactions correctly describe these materials and generate this anisotropy.

In this Letter we answer this question for CrI_3, one of the most robust 2D ferromagnets with a T_C of 45 K for the monolayer [1]. We first construct a general Hamiltonian based on its crystal symmetries containing anisotropic Kitaev K and symmetric off-diagonal Γ interactions in addition to the Heisenberg J interactions. We determine the strength of these interactions using ferromagnetic resonance (FMR).

FMR provides spectroscopically precise measurements of magnetic anisotropy, magnetization, spin-wave modes, and damping [8–10]. The structure of the magnetic anisotropy of a given material can be obtained from angle-dependent FMR by measuring the change in the resonance field as the direction of the external field $\mathbf{H}_0$ is varied [8]. At 2 K, CrI_3 single crystals have a $\sim$3 T anisotropy field H_a oriented normal to the layer plane [11,12]. This large H_a results in a resonance frequency of at least $\omega/2\pi \sim 100$ GHz in an out-of-plane field. We performed angle-dependent FMR using a heterodyne quasi-optical electron spin resonance spectrometer [13]. The measurement was implemented at $\omega/2\pi =$ 120 and 240 GHz and at $T = 5$–80 K. The angle θ_H between $\mathbf{H}_0$ and the e_3 axis normal to the sample plane [see Fig. 1(d)] is varied by rotating the thin CrI_3 single crystal plate about the axis indicated by the orange line in Fig. 1(a). A representative example of the FMR spectra for different θ_H at 240 GHz and 5 K is shown in Fig. 2(a).

The resonance field $H_{\rm res}(\theta_H, \omega, T)$, plotted in Figs. 2(b)–2(g), shows two distinct anisotropy features as θ_H is varied, which we label ΔH_A and ΔH_B in Fig. 2(a): ΔH_A is the shift in $H_{\rm res}$ from the free ion contribution $\omega/\gamma_{\rm Cr}$, where $\gamma_{\rm Cr}$ is the gyromagnetic ratio of Cr^{3+}, and ΔH_B is the difference in $H_{\rm res}$ between θ_H and $180° - \theta_H$. These anisotropy features are crucial to understanding the magnetic behavior of CrI_3 and are central to our symmetry-based theoretical analysis.

In order to analyze the anisotropies measured in FMR and determine the microscopic exchange interactions, we begin by writing the most general Hamiltonian allowed by the symmetries of a monolayer with undistorted CrI_6 octahedra: the crystal lattice is globally invariant under (i) time reversal, (ii) 120° rotations about the e_3 axis at each Cr^{3+} ion, (iii) Cr- Cr-bond-centered spatial inversion, (iv) 180° rotations about the Cr-Cr bonds, and (v) locally

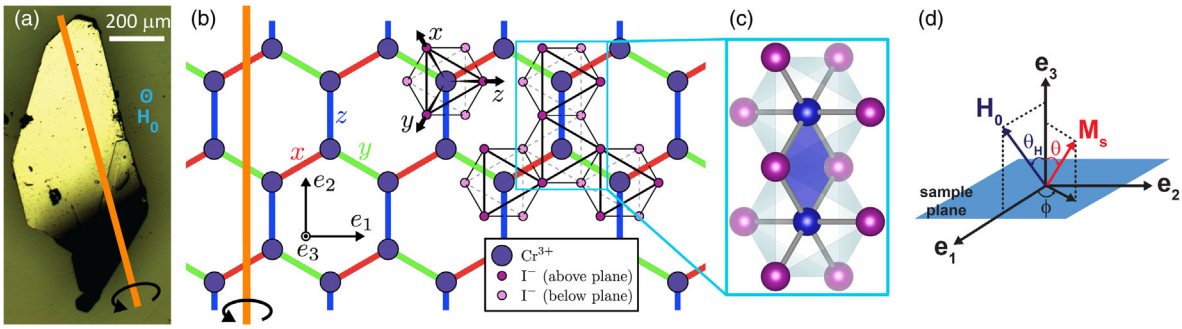

FIG. 1. (a) Optical image of the CrI_3 single crystal for the FMR experiment (axis of rotation shown in orange). The internal angles of the cleaved edges are multiples of 30°. The sample thickness is ~35 μm. (b) Schematic of the honeycomb lattice of the Cr^{3+} ions (dark blue) inside the iodine octahedron (upper: violet, lower: pink). Octahedral coordinate axes x, y, z (black), FMR coordinate axes e_1, e_2, e_3, and Kitaev bonds x (red), y (green), z (blue) are indicated. (c) Pair of neighboring edge-sharing octahedra highlighting the local symmetries and the superexchange plane (blue). (d) FMR coordinate system.

invariant under 180° rotations about the axis perpendicular to a Cr-Cr bond's superexchange plane.

Based on these symmetries, we obtain the general Hamiltonian

$$\mathcal{H} = \mathcal{H}_S + \mathcal{H}_Q - g\mu_B \mathbf{H}_0 \cdot \sum_i \mathbf{S}_i, \tag{1}$$

where

$$\mathcal{H}_S = \sum_{\langle ij\rangle \in \lambda\mu(\nu)} [J\mathbf{S}_i \cdot \mathbf{S}_j + K S_i^\nu S_j^\nu + \Gamma(S_i^\lambda S_j^\mu + S_i^\mu S_j^\lambda)] + \sum_{\langle ij\rangle \in \text{interlayer}} J_\perp \mathbf{S}_i \cdot \mathbf{S}_j \tag{2}$$

describes the spin-spin interactions, $\mathcal{H}_Q$ describes the quadrupole-quadrupole interactions (see Supplemental Material [14]), $\mathbf{S}_i$ is the spin-3/2 operator for the Cr^{3+} ion at site i, $-g\mu_B \mathbf{H}_0 \cdot \sum_i \mathbf{S}_i$ is the Zeeman coupling, g is the g factor of Cr^{3+}, μ_B is the Bohr magneton, and $J_\perp$ is the interlayer Heisenberg coupling [18]. $\langle ij\rangle \in \lambda\mu(\nu)$ denotes that the Cr^{3+} ions at the neighboring sites i, j are interacting via a ν bond, where $\lambda, \mu, \nu \in \{x, y, z\}$.

We next determine the spin interaction parameters in the Hamiltonian. From the resonance field $H_{\text{res}}(\theta_H, \omega, T)$ we determine the value of $J + K/3 = -1.94$ meV, which appears as a combination in mean field theory (MFT) and determines how quickly ΔH_A and ΔH_B shrink with increasing temperature; and $\Gamma = -67.5$ μeV, which determines the size of ΔH_A at low temperatures. The detailed fitting procedure is described in the Supplemental Material [14]. From the switching field ~0.6 T in bilayer CrI_3 [1,3,19] we estimate $|J_\perp| \sim 0.03$ meV, which is negligible compared to $J + K/3$. Remarkably, the high spectroscopic precision of FMR also enables us to estimate the μeV-scale quadrupole interaction constants (listed in Table I), which give rise to ΔH_B in Fig. 2(a). The calculated H_{res} and $M_s(T)$ are in reasonable agreement with the data at all temperatures and frequencies [Figs. 2(b)–2(g)]. From the known $T_C = 61$ K of bulk CrI_3, we then determine the value of $K = -5.2$ meV, which automatically fixes the value of $J = -0.2$ meV [see Fig. 3(a)].

A key finding of our analysis is that the Kitaev interaction is the dominant interaction in CrI_3, almost 25 times stronger than the Heisenberg interaction. A strong signature of this Kitaev interaction in CrI_3 is the ~5 meV Dirac gap (Δ_K) at $\tilde{K}$ in the spin-wave dispersion, as shown in Fig. 3(d), which is corroborated by a recent inelastic neutron scattering experiment [22]. Furthermore, in the absence of the Kitaev interaction, T_C is incorrectly estimated to be 100 K [Fig. 3(a)].

It is important to note that Kitaev anisotropic exchange interactions arise naturally for 2D honeycomb networks of edge-sharing octahedrally coordinated transition metals, as found in CrI_3 and discussed previously in A_2IrO_3 (A = Na, Li) [23,24] and α-$RuCl_3$ [25]. Electrons from a transition metal (TM) cation can hop to a neighboring TM cation via their shared ligands X along two pathways [see Fig. 1(c)] [26–28]. In the presence of strong spin–orbit coupling (SOC) on either the cation, ligand, or both, the destructive interference between competing exchange pathways produce Kitaev interactions and weaken the Heisenberg interaction [29]. Even though the Kitaev interaction leads to frustration, the spin moments in CrI_3 are large ($S = 3/2$), so quantum fluctuations are not strong enough to produce a quantum spin liquid state.

We next construct a Landau free energy functional (FEF) to map out the various magnetic anisotropies in CrI_3 and further connect the coefficients of the Landau FEF to the exchange interaction constants. The Landau FEF based on the underlying symmetries up to sixth order in the direction cosines α, β, γ (the components of the saturation magnetization $\mathbf{M}_s$ along the x, y, z directions) [Fig. 1(b)] is given by [30–32]

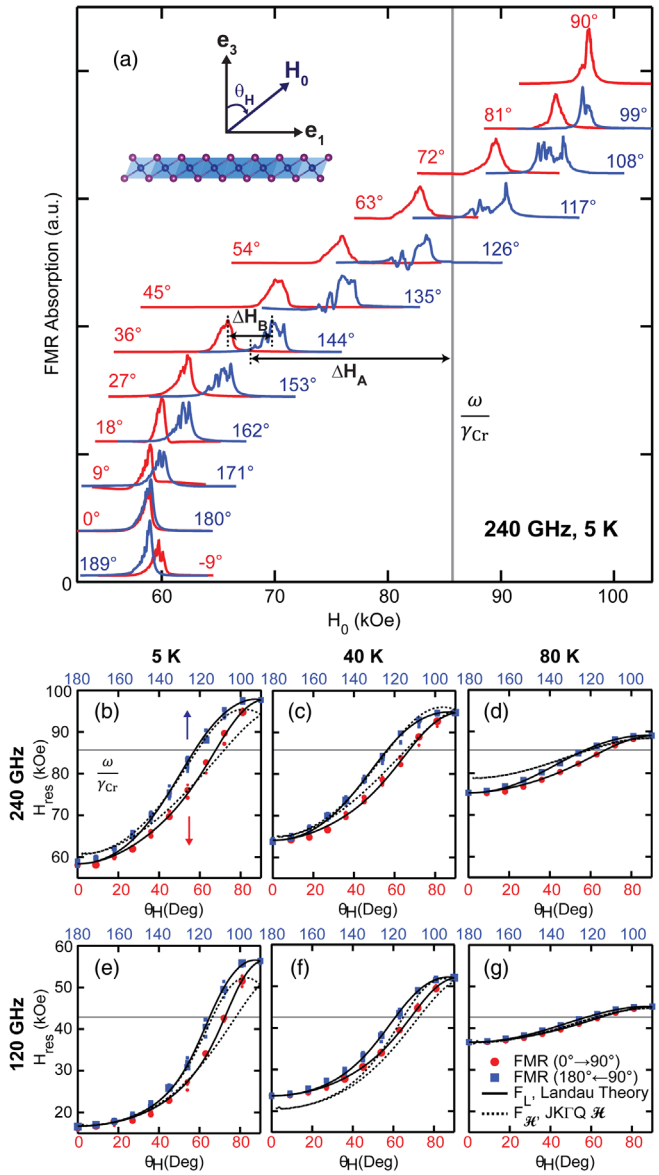

FIG. 2. (a) Evolution of the FMR spectrum as θ_H is varied, measured at 240 GHz and 5 K. Each spectrum is offset and scaled moderately for clarity. The same offset is applied for θ_H and $180° - \theta_H$. ΔH_A and ΔH_B are two anisotropy features in $H_{\rm res}$.$\omega/\gamma_{\rm Cr}$ denotes the corresponding $H_{\rm res}$ for a free ion spin. (b) $H_{\rm res}$ vs θ_H obtained from (a). The marker size indicates the signal peak area in the Lorentzian fits of the FMR spectrum. The red (blue) markers and labels indicate the range of angles from 0° to 90° (90° to 180°). The solid and dashed black lines are fits calculated from Landau theory [Eq. (3)] and MFT of our model Hamiltonian [Eq. (1)], respectively. Similarly, (c)–(g) show $H_{\rm res}$ vs θ_H for various frequencies and temperatures.

$$F_L = 2\pi M_s^2 \cos^2\theta + K_{21}(\alpha\beta + \beta\gamma + \gamma\alpha) + K_{41}(\alpha^2\beta^2 + \beta^2\gamma^2 + \gamma^2\alpha^2) + K_{42}\alpha\beta\gamma(\alpha + \beta + \gamma) + K_{61}\alpha^2\beta^2\gamma^2 + K_{62}(\alpha^3\beta^3 + \beta^3\gamma^3 + \gamma^3\alpha^3) + K_{63}\alpha\beta\gamma(\alpha^3 + \beta^3 + \gamma^3) - \mathbf{M}_s \cdot \mathbf{H}_0, \quad (3)$$

TABLE I. Values of the spin and quadrupole interaction constants in the Hamiltonian for CrI_3 bulk crystals [Eq. (1)] and the angle dependence of the anisotropies they generate in terms of the direction cosines α, β, γ [compare to Fig. 4(c)]. The constants with a subscript Q are the quadrupole interaction constants described in the Supplemental Material [14]. The values are determined experimentally (with uncertainties of ~0.1%) through angle-dependent FMR and the known $T_C = 61$ K.

Coupling constant	Value (μeV)	Angle dependence
J	−212	1
K	−5190	1
Γ	−67.5	$\alpha\beta + \beta\gamma + \gamma\alpha$
$J_Q + K_Q/3$	2.40	$\alpha^2\beta^2 + \beta^2\gamma^2 + \gamma^2\alpha^2$
Γ_Q	−2.69	$\alpha^2\beta^2 + \beta^2\gamma^2 + \gamma^2\alpha^2$, $\alpha\beta\gamma(\alpha + \beta + \gamma)$
Γ'_Q	−0.372	$\alpha\beta + \beta\gamma + \gamma\alpha$, $\alpha^2\beta^2 + \beta^2\gamma^2 + \gamma^2\alpha^2$, $\alpha\beta\gamma(\alpha + \beta + \gamma)$
K'_Q	−0.170	$\alpha^2\beta^2 + \beta^2\gamma^2 + \gamma^2\alpha^2$

where $2\pi M_s^2 \cos^2\theta$ is the shape anisotropy, θ is the angle between $\mathbf{M}_s$ and the e_3 axis [Fig. 1(d)], and $K_{pq}(\omega, T)$ are the coefficients associated with the magnetocrystalline anisotropies plotted in Fig. 4(c). The FEF determines the resonance condition Eq. (S4) of ω and $H_{\rm res}(\theta_H, \omega, T)$ (see Supplemental Material [14]). The values of the $K_{pq}(\omega, T)$ that fit the data are shown in Fig. 4(a), and the corresponding fits are shown in Figs. 2(b)–2(g).

We map out the total Landau FEF F_L shown in Fig. 4(d) using the K_{pq} obtained at 5 K for 240 GHz. We find that the uniaxial term $F_{L,21} = K_{21}(\alpha\beta + \beta\gamma + \gamma\alpha)$ is the dominant anisotropy in CrI_3, having $F_{L,21}(\theta = 90°) - F_{L,21}(\theta = 0°) \sim 220\,\mu$eV/Cr (corresponding to $H_a \sim 2.5$ T), which primarily accounts for the large ΔH_A in Fig. 2(a). The higher-order anisotropy terms (K_{4q}, K_{6q}) in Fig. 4(c) account for the small shift ΔH_B since they are not symmetric about the film plane.

By combining the microscopic spin interaction and Landau theory approaches, we can provide insight into the magnetic anisotropy produced by each interaction in the Hamiltonian [Eq. (1)]. For example, for the Γ interaction we look at the free energy difference

$$\Delta F_\Gamma = F_{\mathcal{H}}(J, K, \Gamma, J_Q, \ldots) - F_{\mathcal{H}}(J, K, 0, J_Q, \ldots), \quad (4)$$

plotted in Fig. 4(e), and compare its angular structure to that of the anisotropies associated with the K_{pq} coefficients in the Landau FEF [plotted in Fig. 4(c)]. We find that Γ is mainly responsible for the large uniaxial anisotropy in CrI_3 associated with K_{21} underlying the ΔH_A. It also plays the crucial role of stabilizing ferromagnetism in a CrI_3 monolayer by opening a ~0.3 meV gap (Δ_Γ) at the zone center $\tilde{\Gamma}$ in the spin-wave spectrum [see Fig. 3(d)]. The much smaller quadrupole terms generate the higher-order anisotropy terms

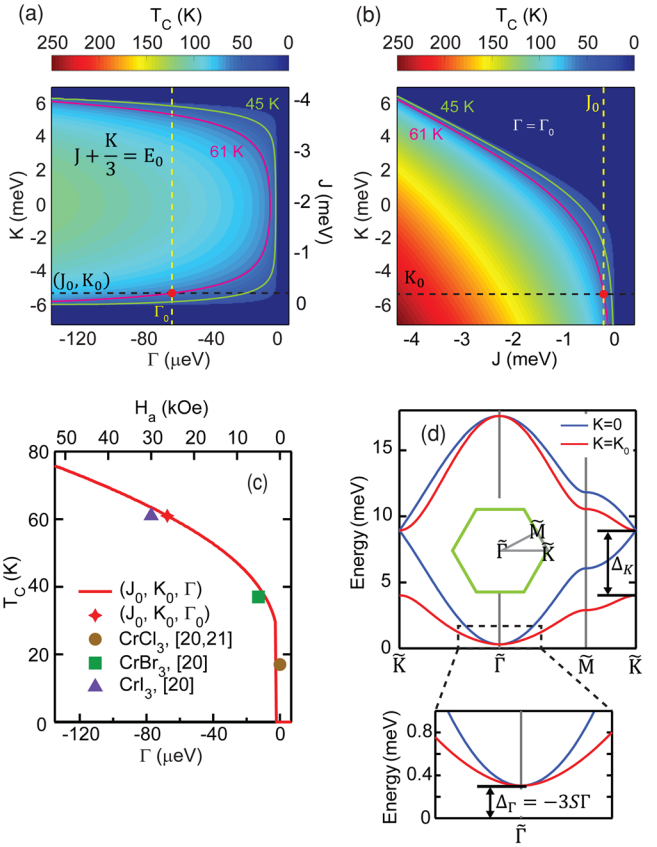

FIG. 3. (a) Dependence of T_C on the spin interaction parameters J, K, Γ under the experimental constraint $J + K/3 \equiv E_0 = -1.94$ meV. (b) Dependence of T_C on J and K for fixed $\Gamma = -67.5$ μeV. In (a) and (b), (J_0, K_0, Γ_0) (filled red circles) are the values of J, K, Γ (listed in Table I) that fit the FMR data and the known $T_C = 61$ K of bulk CrI_3; the magenta and green lines are contour lines for $T_C = 61$ (bulk) and $T_C = 45$ K (monolayer). (c) Dependence of T_C on the anisotropy field H_a (and on Γ) for CrX_3 ($X = \mathrm{Cl, Br, I}$) bulk crystals [20,21]. The values of H_a used are for temperatures mostly below 5 K. (d) Spin-wave dispersion calculation along the momentum-space path $\tilde{K}$–$\tilde{\Gamma}$–$\tilde{M}$–$\tilde{K}$. The blue and red plots correspond to $(J, K, \Gamma) = (E_0, 0, \Gamma_0)$ and (J_0, K_0, Γ_0), respectively. Note that the Kitaev interaction is responsible for opening the gap Δ_K between the bands at the Dirac point $\tilde{K}$. We zoom in on the area in the dashed black box to show the gap $\Delta_\Gamma = -3S\Gamma$ at the zero-momentum point $\tilde{\Gamma}$, where $S = 3/2$ is the spin of the Cr^{3+} ions.

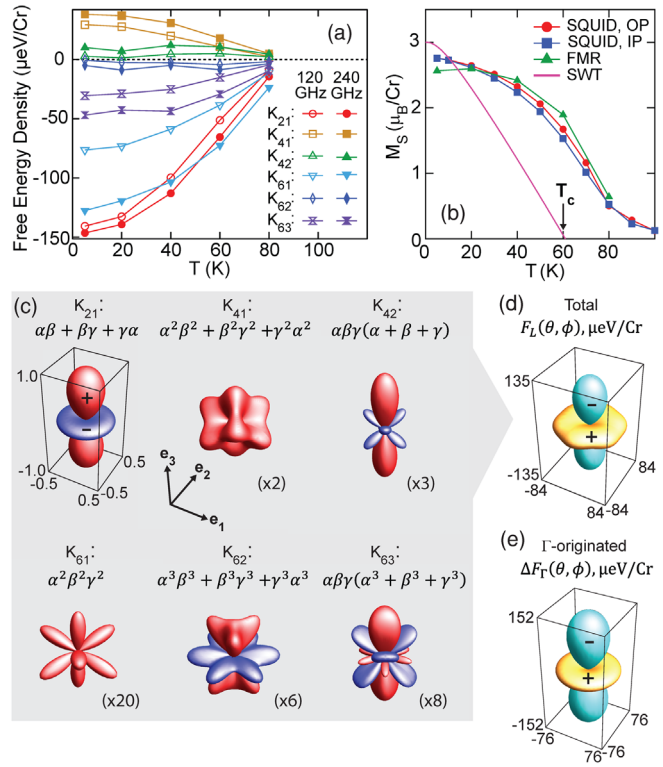

FIG. 4. (a) Temperature dependence of the coefficients K_{pq} associated with the basic anisotropy structures shown in (c) for 120 and 240 GHz. (b) Saturation magnetization $M_s(T)$ obtained from SQUID magnetometry [out of plane (OP) and in plane (IP)], a MFT analysis of the FMR data, and a zero-field spin-wave theory (SWT) analysis using the values of the spin interaction constants found (listed in Table I). In (a) and (b), the lines connecting the markers are guides to the eye. (c) Basic anisotropy structure in terms of the direction cosines α, β, γ (the projections of the magnetization onto the x, y, z directions). The sizes are rescaled relative to that for $\alpha\beta + \beta\gamma + \gamma\alpha$ with the indicated magnifications. Red (blue) denotes positive (negative) values. (d) Total anisotropy FEF F_L for 240 GHz and 5 K constructed from Eq. (3). Orange (cyan) represents positive (negative) values. (e) Contribution of Γ to the FEF, ΔF_Γ, at 5 K. (c)–(e) are plotted with the coordinate axes e_1, e_2, e_3.

associated with K_{4q} and K_{6q} underlying the ΔH_B. Even though J and K generate no magnetic anisotropy, from the MFT estimate $k_B T_C^{\mathrm{MFT}} = -\frac{5}{4}(3J + K + 2\Gamma)$ we see that they determine the scale for T_C since they are much larger than Γ.

Our model also describes the relation between the anisotropy field H_a and T_C for the chromium trihalides ($X = \mathrm{Cl, Br, I}$). By inferring their values of Γ using the low-temperature relation $H_a \simeq -3S^2\Gamma/(M_s V_{\mathrm{Cr}})$ obtained from MFT, where V_{Cr} is the volume per Cr^{3+} ion in CrI_3, we can compare the predicted T_C vs Γ relation using the values of J and K obtained for bulk CrI_3 to the known values of T_C and H_a for bulk CrX_3 [see Fig. 3(c)] [20,21]. We note that although the prediction curve agrees closely with the data for $CrCl_3$ and $CrBr_3$, this does not imply that they have the same J and K as CrI_3; in fact, we expect K to be much weaker in $CrCl_3$ and $CrBr_3$ since Cl^- and Br^- have weaker SOC than I^-.

Given that CrI_3 has a T_C of 61 K for bulk crystals and 45 K for a monolayer, we can speculate on the changes in the values of the spin interaction constants J, K, and Γ that might occur upon exfoliation. A reduction in the strength of one of these interactions by a factor of 2–3 or of several interactions by a smaller amount, perhaps as a result of crystal distortions, would lower T_C by the appropriate amount [see Fig. 3(a) and 3(b)]. FMR studies on monolayer CrI_3 are needed to explore this further.

In conclusion, our symmetry-based theoretical analysis of angle-dependent FMR measurements of single crystal CrI_3 has revealed strong Kitaev interactions in honeycomb CrI_3, almost 25 times larger than the standard Heisenberg exchange, that open a ~5 meV gap at the Dirac points in the magnon dispersion, our prediction that was recently corroborated by an inelastic neutron scattering study of CrI_3 [22]. Such Kitaev interactions arise naturally in edge-sharing octahedra due to SOC and the interference of exchange pathways. We also found a small anisotropic Γ exchange that generates the large magnetic anisotropy in CrI_3, opens a gap at the zone center, and stabilizes ferromagnetic long-range order in two dimensions. This is in contrast to previous studies, which have used Ising anisotropy [4,6,33–36] or single-ion anisotropy [2,18,22,37] to explain this large magnetic anisotropy; however, the former is not allowed by the crystal symmetries of CrI_3, whereas the latter is estimated to be too small [33] due to the weak SOC on the Cr^{3+} ion. Our work also provides insight needed to devise new 2D materials with properties ranging from high-T_C magnetism to quantum spin liquid states.

Angle-dependent FMR and our symmetry-based analysis can readily be applied to other 2D materials in order to correctly characterize their magnetic interactions. In particular, we propose performing these FMR measurements on the $S = 1/2$ Kitaev material α-$RuCl_3$, which like CrI_3 has Kitaev, Heisenberg, and Γ interactions, but whose interaction constants are still hotly debated [38].

We thank W. Zhang for helpful discussions. This work was supported by the Center for Emergent Materials, an NSF-funded MRSEC under Grant No. DMR-1420451. J. E. G. acknowledges the Camille and Henry Dreyfus Foundation for partial support. D. W. gratefully acknowledges the financial support by the German Science Foundation (DFG) under the fellowship No. WE6480/1. Part of this work was performed at the National High Magnetic Field Laboratory, which is supported by NSF Cooperative Agreements No. DMR-1157490 and No. DMR-1644779 and the State of Florida.

I. L. and F. G. U. contributed equally to this work.

*lee.2338@osu.edu
†hammel@physics.osu.edu

[1] B. Huang, G. Clark, E. Navarro-Moratalla, D. R. Klein, R. Cheng, K. L. Seyler, D. Zhong, E. Schmidgall, M. A. McGuire, D. H. Cobden, W. Yao, D. Xiao, P. Jarillo-Herrero, and X. Xu, Nature (London) **546**, 270 (2017).
[2] C. Gong, L. Li, Z. Li, H. Ji, A. Stern, Y. Xia, T. Cao, W. Bao, C. Wang, Y. Wang, Z. Q. Qiu, R. J. Cava, S. G. Louie, J. Xia, and X. Zhang, Nature (London) **546**, 265 (2017).
[3] S. Jiang, L. Li, Z. Wang, K. F. Mak, and J. Shan, Nat. Nanotechnol. **13**, 549 (2018).
[4] D. R. Klein, D. MacNeill, J. L. Lado, D. Soriano, E. Navarro-Moratalla, K. Watanabe, T. Taniguchi, S. Manni, P. Canfield, J. Fernández-Rossier, and P. Jarillo-Herrero, Science **360**, 1218 (2018).
[5] S. S. Pershoguba, S. Banerjee, J. C. Lashley, J. Park, H. Ågren, G. Aeppli, and A. V. Balatsky, Phys. Rev. X **8**, 011010 (2018).
[6] J. Liu, M. Shi, P. Mo, and J. Lu, AIP Adv. **8**, 055316 (2018).
[7] N. D. Mermin and H. Wagner, Phys. Rev. Lett. **17**, 1133 (1966).
[8] M. Farle, Rep. Prog. Phys. **61**, 755 (1998).
[9] R. D. McMichael, D. J. Twisselmann, and A. Kunz, Phys. Rev. Lett. **90**, 227601 (2003).
[10] I. Lee, Y. Obukhov, G. Xiang, A. Hauser, F. Yang, P. Banerjee, D. V. Pelekhov, and P. C. Hammel, Nature (London) **466**, 845 (2010).
[11] M. A. McGuire, H. Dixit, V. R. Cooper, and B. C. Sales, Chem. Mater. **27**, 612 (2015).
[12] J. F. Dillon and C. E. Olson, J. Appl. Phys. **36**, 1259 (1965).
[13] J. van Tol, L.-C. Brunel, and R. J. Wylde, Rev. Sci. Instrum. **76**, 074101 (2005).
[14] See Supplemental Material at http://link.aps.org/supplemental/10.1103/PhysRevLett.124.017201 for detailed information of samples, experiment, and theoretical analysis, which includes Refs. [11,15–17].
[15] D. Shcherbakov, P. Stepanov, D. Weber, Y. Wang, J. Hu, Y. Zhu, K. Watanabe, T. Taniguchi, Z. Mao, W. Windl, J. Goldberger, M. Bockrath, and C. N. Lau, Nano Lett. **18**, 4214 (2018).
[16] W.-B. Zhang, Q. Qu, P. Zhu, and C.-H. Lam, J. Mater. Chem. C **3**, 12457 (2015).
[17] J. Smit and H. G. Beljers, Philips Res. Rep. **10**, 113 (1955).
[18] A. Narath, Phys. Rev. **140**, A854 (1965).
[19] S. Jiang, J. Shan, and K. F. Mak, Nat. Mater. **17**, 406 (2018).
[20] M. McGuire, Crystals **7**, 121 (2017).
[21] B. Kuhlow, Phys. Status Solidi (a) **72**, 161 (1982).
[22] L. Chen, J.-H. Chung, B. Gao, T. Chen, M. B. Stone, A. I. Kolesnikov, Q. Huang, and P. Dai, Phys. Rev. X **8**, 041028 (2018).
[23] Y. Singh, S. Manni, J. Reuther, T. Berlijn, R. Thomale, W. Ku, S. Trebst, and P. Gegenwart, Phys. Rev. Lett. **108**, 127203 (2012).
[24] H. Gretarsson, J. P. Clancy, X. Liu, J. P. Hill, E. Bozin, Y. Singh, S. Manni, P. Gegenwart, J. Kim, A. H. Said, D. Casa, T. Gog, M. H. Upton, H.-S. Kim, J. Yu, V. M. Katukuri, L. Hozoi, J. van den Brink, and Y.-J. Kim, Phys. Rev. Lett. **110**, 076402 (2013).
[25] A. Banerjee, C. A. Bridges, J.-Q. Yan, A. A. Aczel, L. Li, M. B. Stone, G. E. Granroth, M. D. Lumsden, Y. Yiu, J. Knolle, S. Bhattacharjee, D. L. Kovrizhin, R. Moessner, D. A. Tennant, D. G. Mandrus, and S. E. Nagler, Nat. Mater. **15**, 733 (2016).
[26] G. Jackeli and G. Khaliullin, Phys. Rev. Lett. **102**, 017205 (2009).
[27] J. G. Rau, Eric Kin-Ho Lee, and H.-Y. Kee, Phys. Rev. Lett. **112**, 077204 (2014).
[28] H.-S. Kim, V. Vijay Shankar, A. Catuneanu, and H.-Y. Kee, Phys. Rev. B **91**, 241110 (2015).
[29] P. P. Stavropoulos, D. Pereira, and H.-Y. Kee, Phys. Rev. Lett. **123**, 037203 (2019).

[30] J. H. van Vleck, Phys. Rev. **52**, 1178 (1937).
[31] C. Zener, Phys. Rev. **96**, 1335 (1954).
[32] E. Ascher, Helv. Phys. Acta **39**, 466 (1966).
[33] J. L. Lado and J. Fernández-Rossier, 2D Mater. **4**, 035002 (2017).
[34] J. Liu, M. Shi, J. Lu, and M. P. Anantram, Phys. Rev. B **97**, 054416 (2018).
[35] F. Zheng, J. Zhao, Z. Liu, M. Li, M. Zhou, S. Zhang, and P. Zhang, Nanoscale **10**, 14298 (2018).
[36] W. Jin, H. H. Kim, Z. Ye, S. Li, P. Rezaie, F. Diaz, S. Siddiq, E. Wauer, B. Yang, C. Li, S. Tian, K. Sun, H. Lei, A. W. Tsen, L. Zhao, and R. He, Nat. Commun. **9**, 5122 (2018).
[37] C. Xu, J. Feng, H. Xiang, and L. Bellaiche, Comput. Mater. Sci. **4**, 57 (2018).
[38] S. M. Winter, A. A. Tsirlin, M. Daghofer, J. van den Brink, Y. Singh, P. Gegenwart, and R. Valentí, J. Phys. Condens. Matter **29**, 493002 (2017).